ACCEPTED MANUSCRIPT

Surface Ionization Waves Propagating over Non-Planar Substrates: Wavy Surfaces, Cut-Pores and Droplets

Surface Ionization Waves Propagating over Non-Planar Substrates: Wavy Surfaces, Cut-Pores and Droplets

Kseniia Konina[1], Juliusz Kruszelnicki[1,4] Mackenzie E. Meyer[2] and Mark J. Kushner[3,5]

[1] Department of Nuclear Engineering and Radiological Sciences, University of Michigan, 2355 Bonisteel Blvd., Ann Arbor, Michigan 48109-2104, USA kseniiak@umich.edu, jkrusze@umich.edu

[2] Applied Physics Program, University of Michigan, 450 Church St., Ann Arbor, MI 48109 USA maemeyer@umich.edu

[3] Department of Electrical Engineering and Computer Science, University of Michigan, 1301 Beal Ave., Ann Arbor, Michigan 48109-2122, USA, mjkush@umich.edu

[4] Present address: KLA Corporation, 1200 Woodridge Ave, Ann Arbor, Michigan, 48105 USA

[5] Author to whom correspondence should be addressed.

Abstract

Atmospheric pressure plasmas intersecting with dielectric surfaces will often transition into surface ionization waves (SIWs). Several applications of these discharges are purposely configured to be SIWs. During propagation of an SIW over the dielectric surface, the plasma charges the surface while responding to changes in geometrical and electrical material properties. This is particularly important for non-planar surfaces where polarization of the dielectric results in local electric field enhancement. In this paper, we discuss results from computational investigations of negative and positive SIWs propagating over nonplanar dielectrics in three configurations – wavy surfaces, cuts through porous materials and water droplets on flat surfaces. We found that negative SIWs are particularly sensitive to the electric field enhancement that occurs at the crests of non-planar surfaces. The local increase in ionization rates by the electric field enhancement can result in the SIW detaching from the surface, which produces non-uniform plasma exposure of the surface. Positive SIWs tend to adhere to the surface to a greater degree. These trends indicate that treatment of pathogen containing droplets on surfaces may be best performed by positive SIWs. The same principles apply to the surfaces cut through pores. Buried pores with small openings to the SIW may be filled by plasma by either flow of plasma into the pore (large opening) or initiated by photoionization (small opening), depending on the size of the opening compared to the Debye length.

1

I. Introduction

The interaction of pulsed atmospheric plasmas with dielectric surfaces typically evolves at some point into propagation of a surface ionization wave (SIW) [1,2]. An example of a volumetric plasma streamer transitioning into a SIW occurs in a dielectric barrier discharge (DBD). In a DBD, a volumetric plasma streamer oriented perpendicular to the bounding dielectric material evolves into a *surface hugging* ionization wave [3]. This SIW is often referred to as the foot of the streamer in a DBD [4]. SIWs are the intended mode of propagation of atmospheric pressure plasmas in applications including plasma actuators for affecting air flow over surfaces [5], ignition sources for plasma aided combustion [6] and treatment of water contaminated with surfactant-like molecules [7].

The development and propagation of a SIW is a consequence of charging of the surface and electric field enhancement at the interaction of the plasma and the dielectric [8]. In order for the SIW to propagate parallel to the surface, there must be an electric field component parallel to the surface. Again referring to the example of the DBD or a plasma jet striking a surface, the applied electric field is initially perpendicular to the surface. The intersection of the bulk plasma streamer normal to the surface electrically charges the dielectric surface at the site of the intersection [3,9]. The surface charge density generates electric field components parallel to the surface that supports propagation of the SIW [10,11]. Once propagating along the surface, there is charge separation at the head of the SIW analogous to the charge separation in the head of a streamer propagating in a bulk gas. This charge separation produces the electric field that avalanches the gas to propagate the SIW [12]. However, the charging of the underlying dielectric maintains propagation along the surface [13].

At the same time, there is a discontinuity in relative permittivity between the underlying dielectric and the plasma, with the permittivity of the dielectric being larger. This discontinuity intensifies the electric field at the surface of the dielectric due to polarization of the surface material, which enhances propagation of the SIW [14]. The region near the head of the SIW is constituted of a conductive column of plasma, an insulating surface of the dielectric substrate and the ambient air – therefore, resembling an electrical triple-point [15]. Additional electric field enhancement is therefore produced.

The propagation of the SIW along the surface can also be viewed as the continuous charging of the capacitance of the surface. Charge is removed from the streamer to charge the local

surface capacitance, C_s (F/cm^2), of the underlying dielectric. This charging of the dielectric locally transfers voltage to the dielectric. This voltage was previously dropped across the gas phase and partially across the head of the SIW. The locally charged dielectric produces an electric field pointing towards the uncharged dielectric ahead of the SIW, which then supports the propagation of the SIW. However, removal of voltage from the SIW to charge the dielectric also weakens the SIW. There are other subtleties that influence the propagation of SIWs, including secondary electron emission due to ion bombardment, photoelectron emission from the surface, photon induced conductivity and kinetic effects in the intense electric fields near the surface [16]. The latter can produce sheath accelerated secondary electrons.

The propagation of the SIW and charging of the dielectric can be described in terms of approaching the saturation charge [17,18]. The saturation surface charge is that value when the normal component of the electric field in the dielectric is supported by the surface charge, σ_s, while in comparison, the normal electric field in the plasma is zero. That is, $\varepsilon_0 E_{np} + \varepsilon_d E_{nd} = \sigma_s \rightarrow \varepsilon_d E_{nd} = \sigma_s$ where E_{np} is the normal component of electric field in the plasma (pointing away from the surface) and E_{nd} is the normal component of electric field in the dielectric have permittivity ε_d. After an SIW has propagated across a surface, the surface charge approaches its saturation value.

The charging of the underlying dielectric by the SIW impacts the speed of the discharge across the surface. The SIW requires more time to charge larger C_s and so the speed of the SIW across the dielectric surface decreases with increasing C_s, as Li et al. has shown by modeling [19]. 2-dimensional simulations were performed by Pechereau, et al [20] of a streamer in air intersecting a flat dielectric slab and transitioning to a SIW. The speed of the SIW increased over thicker slabs for the same permittivity, a result of C_s being smaller for thicker dielectrics. For the same thickness dielectric, the SIW speed was lower with larger dielectric constant (larger C_s). Although the speed of the SIW depends on C_s, secondary electron emission processes by ions and photons from the dielectric are less influential [16].

The discussion to this point applies to the propagation of SIWs on planar dielectrics. The propagation of SIWs on non-planar dielectrics has additional complexity due to the electric field enhancement at the convex curvature of the dielectrics. High permittivity dielectric materials expel electric field into bounding materials having a lower permittivity. As a result, electric field enhancement occurs at the apex of convex protrusions of dielectrics in the same manner as electric

enhancement occurs at the edges of metal electrodes.

A second complication for SIWs propagating on non-planar dielectrics results from shadowing of ionizing radiation. The propagation of a positive SIW depends on photoionization in front of the head of the SIW in the same way that photoionization supports the propagation of positive streamers in the bulk gas. Non-planar geometries can shadow the photons originating in the head of the SIW from illuminating and photoionizing the region adjacent to the surface in front of the SIW. This lack of preionization due to shadowing of the photon-flux can lead to a distinctive difference in propagation properties of positive and negative SIWs.

The propagation of SIWs on planar surfaces has been well characterized while there have been limited quantitative investigations of the propagation of SIW on non-planar surfaces. In this context, non-planar refers to surfaces in which the local topology (e.g., roughness or waviness of the surface) has dimensions that are commensurate with that of the SIW. The diameter of atmospheric pressure streamers and thickness of SIWs are up to hundreds of microns [21,22]. This spatial scale is the order of non-planarity that we are concerned with.

Meyer et al. [18] measured and modeled positive SIWs propagating in atmospheric pressure air across flat and profiled dielectric surfaces ($\varepsilon_r = 3.17$) consisting of shallow troughs (or corrugations) having a period of 1.79 mm and depth of 0.514 mm. For positive streamers produced by a 35 kV pulse having a 420 ns risetime, the positive SIW adhered to the profiled surface, propagating with speed of 1.8×10^8 cm/s, about 15% slower than over the equivalent flat surface. Ning et al. [23] performed 2-dimensional modeling of a plasma jet sustained in atmospheric pressure He/N$_2$=99.5/0.5 flowing into ambient air onto a wavy dielectric surface consisting of alternating semi-circles with a radius of 0.2 mm and crest-to-crest period of 0.8 mm. The plasma jet strikes the surface as a bulk Ionization Wave (IW), and transitions to a SIW propagating radially outward. Positive SIWs nearly uniformly penetrated into the grooves of the surface, limited by a cathode-fall like sheath at the surface. Negative streamers filled the grooves directly under the plasma jet. However, when transitioning to a surface wave, the negative SIW did not fully adhere to the surface. Fluxes of radicals and ions were then more uniform across the surface for positive SIWs compared to negative SIWs. In simulations of a He/N$_2$ dielectric barrier discharge with one of the dielectrics being wavy, Wang et al. [24] found differential charging of the surface. The crests of the waves tend to charge negatively while the grooves tend to charge positively.

One configuration of a non-planar surface is a curved, but smooth, dielectric. Single

4

filament experiments in a DBD having a single or a pair of hemispherical dielectric covered electrodes have shown propagation of SIWs along the smooth, curved surface that are qualitatively similar to those on strictly planar surfaces [12,25]. Optical emission was measured in a DBD by Mujahid in which the dielectric covering the grounded electrode consisted of an array of touching hemispheres [26,27]. Initiating plasma filaments intersected the apex of the hemispheres due to electric enhancement and polarization of the dielectric, followed by SIWs which propagated down the slopes of the hemispheres. Sun et al experimentally and computationally investigated SIWs propagating along a curved polyimide surface sustained with alternating powered and grounded electrodes buried in the dielectric [28]. They found that bending of the thin (100 μm) polymer sheet from being concave to the plasma to convex to the plasma increased electron densities by as much as 30%.

Wang et al. [29] computationally investigated the propagation of positive SIWs in air across profiled dielectrics with concave indentations (what we will call cut-pores) and convex protrusions. They found that for indentations 1 mm wide and 0.2 mm or 0.3 mm deep, the SIW conformally propagated into and out of the indentation. However, the photoionization source in front of the streamer, a measure of the ionization rate in the stream head, was modulated as the SIW propagated into and out of the indentations.

In this paper, we discuss results from a computational investigation of the propagation of SIWs over non-planar dielectric surfaces sustained in atmospheric pressure humid air. The non-planar structures are waves in the surface, cut-pores and water droplets on a flat dielectric. This investigation was performed with a 2-dimensional plasma hydrodynamics model. We found that changes in surface topology on the order of the thickness of the SIW can significantly affect the propagation of the SIW in a manner that is dependent on the polarity of the voltage. Negative SIWs will follow and adhere to the wavy surface for moderate heights of the waves. However, beyond a critical height of the wave, electric field enhancement at the apex of the wavy-surface will launch bulk ionization waves (IWs) away from the surface, producing a hopping-behavior from one wave crest to another. Reverse ionization waves will also occur due to charging of the surface. Positive SIWs will adhere to the surface even for large amplitudes of the wavy surface. However, these SIWs will sometimes stall due to shadowing of the photoionization that sustains the SIW. This hopping-vs-adhering nature of the SIWs results in different exposure of the surface to the plasma. Surfaces under negative SIWs that detach are less uniformly exposed to plasma

5

fluxes and VUV radiation than surfaces under positive SIWs. This difference in exposure extends to SIWs propagating over droplets on flat surfaces. SIWs propagating over cut pores were also investigated. These interactions are also dominated by electric enhancement by curvature of the surface and charging, producing hopping of the SIW over the exposed surfaces of the pores. Plasma leakage into subsurface pores that are connected to the plasma through small openings is largely determined by the size of the opening being larger than or smaller than the local Debye length.

The model used in this investigation is described in Section II. SIWs propagating over wavy dielectric surfaces are discussed in Section III, and propagating over cut-pores in Section IV. The implications of these results for SIWs propagating over droplets on flat surfaces are discussed in Section V. Our concluding remarks are in Section VI.

II. Description of the Model

The model used in this investigation is *nonPDPSIM*, a 2-dimensional plasma hydrodynamics simulation executed on an unstructured mesh. *nonPDPSIM* has been described in previous publications [30,31] and so will only those options and modules used in this investigation will be briefly discussed here.

The implementation of *nonPDPSIM* used here, algorithms and reaction mechanisms, is essentially the same as described in Ref. [31]. Partial differential equations for the densities and temperatures of charged and neutral species are integrated in time, simultaneously with the solution of Poisson's equation for the electric potential. Densities, potentials and temperature are solved at the mesh points whereas fluxes are produced along the chord between mesh points. Continuity equations for charged species (electrons, positive ions and negative ions) are formulated using the Scharfetter-Gummel (SG) formulation for fluxes between the mesh points. SG fluxes are drift-diffusion expressions that automatically select upwind-or-downwind expressions as appropriate. Divergence terms in the continuity equations are formulated using conservative finite volume techniques. Neutral particle densities are obtained from continuity equations employing only diffusive fluxes. Due to the short duration of the simulations discussed here, bulk gas flow and changes in gas temperature were not solved for. For simulations of SIWs propagating over water droplets, the reaction mechanism for air-plasmas reacting with water is essentially the same as in Ref. [32].

The electron temperature is obtained from an electron energy conservation equation with contributions from joule heating; elastic, inelastic and superelastic collisions with atoms and molecules; non-electron heating sources (e.g., Penning ionization, photo-ionization); and thermal conduction. Electron impact rate and transport coefficients as a function of average electron energy (or temperature) are provided by stationary solutions for Boltzmann's equation for the electron energy distribution.

Poisson's equation is solved for the electric potential while including charge densities in the gas phase, on surfaces and in materials. Surface charge densities, ρ_s, are generally provided by

$$\frac{\partial \rho_s}{\partial t} = \sum_j -\nabla \cdot q_j \Phi_j + \sum_j \nabla \cdot q_e \Phi_j \gamma_j - \nabla \cdot \vec{j}_c - \nabla \cdot \vec{j}_E \qquad (1)$$

where the terms on the right had side are for collection of charge on the surface from species j having charge q_j and flux Φj; secondary emission of electrons due to ions, neutrals and photons having electron emission coefficient γ_j; conduction current j_c from the surface through the material, and electric field emission current j_E. The conduction current density in the material is $\vec{j}_c = \sigma_m \vec{E}$ where σ_m is the conductivity of the material. Electric field emission from surfaces is given by the Fowler-Nordheim expression for thermionically enhanced emission,

$$j_E = AT^2 \exp\left(-\left(\Phi_W - \sqrt{q^3 E/\varepsilon_0}\right)/\left(k_B T\right)\right), \qquad (2)$$

where A is the Richardson-Dushman constant (120.13 A/cm^2-K^2), T is the temperature of the surface, Φ_W is the work function of the surface, k_B is Boltzmann's constant, q is the elementary charge, and E is the electric field at the surface of.

The duration of the simulations varied with conditions. The simulations were terminated when the SIW traversed the computational domain, which required 5 ns to 25 ns depending on the voltage and structure; as well as positive or negative SIW. For those cases where fluences to the surface (time integral of flux) were compared, the simulations were conducted for about the same time and well after the SIW passed over the regions of interest. The flux was integrated for the duration of the simulations. The flux to the surface decreased by factors of 10-100 after the SIW passed, and so the majority of fluence was accounted for in spite of small differences in integration times.

III. SIW Propagation Over Non-Planar Wavy Surfaces

Although the transition from a bulk plasma streamer to a SIW upon intersecting a dielectric is intrinsically interesting and important, the emphasis in this paper is on the propagation of sustained SIWs. In this regard, a geometry was chosen akin to a plasma actuator in which a SIW is launched from a coaxial electrode directly onto the surface. This configuration was motivated by the work of Kettlitz, et al [21]. The 2-dimensional Cartesian model geometry is show in Fig. 1a. The powered electrode having a tip with radius of curvature of 20 μm is in contact with a dielectric having a relative permittivity of $\varepsilon_r = 10$. The dielectric is 300 μm thick and rests on a grounded electrode which wraps around the computational domain, having a height of 0.5 cm and length of 0.8 cm. There is an insulating break between the ground and powered surfaces. The vertical dielectric section on the right-hand-side is to prevent SIWs that traverse the computational domain from directly touching ground and arcing. The secondary electron emission coefficient for all positive ions on the dielectric was $\gamma = 0.15$. The gas was humid air ($N_2/O_2/H_2O = 78/21/1$) at 1 atm (760 Torr) and 300 K. In order to decrease the computational load, the gas volume between the top electrode and dielectric was divided into a region that was modeled as a true gas and a region that was modeled as a dielectric with a relative permittivity of $\varepsilon_r = 1.0$. We confirmed that we received the same results using this approach as representing the entire domain as gas. Photo-electron emission from the dielectric produced by incident VUV radiation was included with probability $\gamma_{ph} = 0.01$.

A spot of neutral plasma having a density of 10^{12} cm^{-3} and 50 μm in diameter was placed at the tip of the powered electrode to seed the discharge. Voltage was applied to the electrode with a linear ramp over 1 ns to a constant voltage to launch the SIW. Structure in the surface of the dielectric was imposed starting 2.5 mm from the tip of the electrode at a location where the SIW would propagate on planar surface in a quasi-continuous manner. The initial structure that was investigated consists of ridges or waves in the dielectric having a period of 300 μm and height (maximum height – minimum height) of flat to $\Delta h = 550$ μm.

The electron density, electron impact ionization source, electron temperature, electric field and photoionization source are shown in Fig. 2 adjacent to the surface for a negative SIW launched with a voltage of –12 kV. This particular image is for 2 ns after the voltage is applied, but is representative of the quasi-continuous properties of the propagating SIW. The thickness of the SIW is about 100 μm with a maximum electron density of 4×10^{15} cm^{-3} with a propagation speed

8

across the surface of 1×10^8 cm/s. The SIW is sustained by an electron impact ionization source with maximum value of 1×10^{25} cm^{-3}s^{-1}. The electric field in the space charge enhanced head of the SIW is 140 kV/cm (or E/N = 570 Td, 1 Td = 10^{-17} V-cm^2), sustaining an electron temperature of 5.4 eV. The electron impact ionization source in the plasma layer behind the head of the SIW is negative, where the E/N < 150 Td. The plasma layer is sustained to some degree by photoionization of O_2 and H_2O from the high lying states of N_2.

Reported speeds of SIW vary significantly, with the applied voltage waveform, location of ground planes, permittivity of the dielectric, surface capacitance C_s (F/cm^2) and type of gas. Kettlitz et al. [21] measured speed of propagation of negative SIWs across alumina in synthetic air at 1 atm of 8×10^6 cm/s, albeit for a slow rising voltage pulse (10 µs) of lower peak amplitude (9 kV). At about 80% the applied E/N used here, Stepanyan measured a negative SIW propagation speed (diffusive mode) in high pressure air of 6×10^7 cm/s [6]. Goldberg et al. measured speeds of 1×10^8 cm/s for SIW over alumina sustained in H_2 at 200 Torr [33] with 3 kV, which would correspond to about 11.4 kV at atmospheric pressure. Also at low pressure, 20 Torr N_2, Petrishchev et al. measured initial SIW speeds over quartz of 1×10^8 cm/s for a -12 kV pulse having a 100 ns rise time.[34] Using an actuator, strip-line geometry, Huang et al. [35] measured speeds of SIW in air over epoxy resin (ε_r = 4.3) of 3×10^7 cm/s for an applied voltage of 14 kV with a 200 ns rise time. Li et al., simulating high voltage SIWs in air, predicted speeds of negative waves of up to 3×10^8 cm/s [19].

As the SIW passes over the dielectric, the capacitance of the dielectric is charged, which transfers much of the applied voltage into the dielectric. For example, 1 mm behind the head of the SIW, the potential of the surface of the dielectric is -7.1 kV, compared to the applied voltage of -12 kV. The electric field inside the dielectric 50 µm below the surface is 250 kV/cm, pointing upwards towards the negative surface charge. The electric field in the gas at the surface of the dielectric has a significant component parallel to the surface at the head of the SIW. As the SIW passes and negatively charges the underlying dielectric, the orientation of the electric field becomes vertical. The negative charging of the dielectric is about -1.1 $\times 10^{15}$ q-cm^{-3}, with a positive space charge layer above the surface of (2-3) $\times 10^{13}$ q-cm^{-3}.

Several numerical experiments were conducted to determine contributing factors to the propagation of the SIW. Photoelectron emission from the surface due to VUV produced by the SIW was included and removed. The secondary electrons from the surface produced by photo-

ionization and by ion bombardment were treated using a kinetic Monte Carlo Simulation. Neither of these processes or procedure had a significant effect on the propagation of the SIW due to the surface appearing to be anode-like, electric fields generally oriented in a manner that accelerates secondary electrons back into the surface.

Electron densities are shown in Fig. 3 for a cathode potential of -12 kV with varying modulation of the surface having total heights (maximum – minimum height of the surface) of $\Delta h = 0$, 50, 100, 200, 400 and 550 μm, and period of 300 μm. The SIW remains in nearly conformal contact with the surface for Δh up to about 150 μm. For an amplitude of $\Delta h = 100$ μm, there is a significant increase in electron density at the apex of the modulation compared to the valley. Due to polarization of the dielectric at the curved surface of the apex, the E/N in the adjacent gas prior to arrival of the SIW is about 30% larger (350 Td) compared to that on the flat surface (270 Td), and more than three times that in the base of the valley of the dielectric (110 Td). This local increase in E/N provides for a larger ionization source near the apex, while the electric enhancement along the surface is still large enough to guide the SIW conformally. The end result is that the electron density at the apex is about twice that in the valley.

As the amplitude Δh of the modulation increases, the SIW detaches from the surface. The detachment is first significant for a wave amplitude of the surface of $\Delta h = 200$ μm. With the additional electric enhancement due to the smaller radius of curvature of the apex of the wavy surface, the E/N in the adjacent gas prior to arrival of the SIW is 440 Td. This value of E/N is sufficient to launch a bulk plasma ionization wave (IW) into the gas. Once this bulk IW is launched from the apex, space charge separation in the head of the IW sustains the wave. The IW is directed towards the vertical surface of the next period of the wavy surface due to the orientation of the electric field being largely normal to the dielectric. This direction of the electric field aligns with the direction of propagation of the bulk IW.

With larger amplitudes of the waves and smaller radius of curvature of apex of the wavy surface, the electric enhancement at the apex of the surface increases. For the surface with amplitude of $\Delta h = 400$ μm, the values of E/N in the gas prior to arrival of the ionization wave at the first, second and third apexes are 460 Td, 300 Td and 205 Td, with the decrease being a consequence of the apexes being further from the cathode but also being shadowed by prior apexes. As electron diffusion ahead of the SIW approaches the apex, these values of E/N are able to launch bulk IWs across the valley of the wavy surface. These IWs are attracted to the electric field enhancement at

10

the next apex. The IW then propagates from apex to apex. (The SIW propagating into the valley is discussed below.) The face of the surface that is shadowed (facing towards the right) is not directly covered by the SIW. The IW launched from the third apex is directed towards the electric field enhancement at the corner of the surface and translates back to a SIW on the following flat surface.

The increase in density of the plasma near the apex of the wavy surface also leads to an increase in production of reactive species. For example, at the same distance from the cathode after passage of the SIW, the density of atomic nitrogen is 3.5×10^{15} cm^{-3} at the first crest of the wave for the $\Delta h = 550$ μm surface compared 1.2×10^{15} on the planar surface. Although these differences in maximum values are not large, the disparity in uniformity of plasma exposure to the surface is large.

The end result of the SIW hopping from peak-to-peak on the wavy surface is a non-uniform plasma exposure of the surface. This lack of uniformity is demonstrated by the fluences of electrons and VUV photons incident onto the surface for modulations of $\Delta h = 50$ μm, 100 μm and 400 μm shown in Fig. 4. (Fluences are the time integrated fluxes.) For a negative SIW, electrons are initially accelerated into the surface, producing charging of the surface which enables propagation of the SIW. Electron fluence to the surface is therefore an indication of the passage of the SIW over that point. The VUV photon flux has a mean free path of only tens of microns, and is produced (in this model) by high lying excited states of N_2 have a threshold energy of 12.25 eV. As a result, these states are dominantly produced by the passage of the head of the SIW (where the electron temperature peaks) as the SIW passes over a surface point. In Fig. 4, the position coordinate refers to the location on the surface from the start of the wavy surface (A) to the end of the wavy surface (E). The locations of the peaks of the modulation (B, C, D) are noted in the insets.

For the SIW propagating over the surfaces having $\Delta h = 50$ μm and 100 μm (Figs. 4a,b), the fluences of electrons and ions are uniform across the surface within a factor of 2. The general trend is a decrease in fluence of electrons and VUV photons from left-to-right, a consequence of a weakening of the SIW resulting from previous charging of the dielectric. Voltage that would have been dropped across the head of the SIW to sustain a high rate of ionization was removed to charge the underlying dielectric. Even with Δh as small as 50 μm, there is modulation in the fluences that result from the polarization of the dielectric and resulting electric field enhancement that occurs around any positive curvature of the surface. The fluences for both heights are maximum just prior

11

to the apex of the wavy surface. These maxima reflect that the electron density is maximum at the location where the polarization in the electric field increases as the curvature transitions to being positive. Although less clear for $\Delta h = 50$ μm in the electron densities shown in Fig. 3, the electron densities favor the leading slope of the curvature for $\Delta h = 100$ μm. For this height in modulation, there is already some "lifting" of the SIW off the surface that reduces fluences on the trailing slope.

For the SIW propagating over the surface having $\Delta h = 400$ μm, there are regions of the surface that have essentially no electron or VUV fluences (Fig. 4c). These regions are on the trailing slope of the wavy surface (facing to the right) where the SIW has "hopped" from one peak to another, shown by the electron densities in Fig. 3e. The SIW directly propagates up the leading slope of the first crest of the wavy-surface. However, for subsequent waves, the surface is exposed to the plasma by a downward, reverse propagating SIW, as discussed below.

The fluences of electrons are 10^{12}-10^{13}/cm^2, as these are the fluences that are required to charge the capacitance of the dielectric to approximately the applied potential. (The fluence of VUV photons is about 100 times larger.) For example, for $\Delta h = 400$ μm, the capacitance is about 30 pF/cm^2 on the flat surface prior to the wavy structures. The potential of the surface is charged from an initial value of -610 V to a final value of -9430 V for an applied potential of -12 kV. Such charging would ideally require a fluence of electrons of 2×10^{12} cm^{-2}. The fluences of electrons here are somewhat higher than that minimum value because of photo-electron emission from the surface (with photo-electron emission coefficient of 0.01) which serves to charge the surface positively, and to a lesser degree secondary electron emission by ions. With VUV fluences of mid-10^{14} cm^{-2}, approximately 10^{12} electrons/cm^2 are removed from the surface. With application of a negative voltage, these electrons are largely accelerated back into the surface to negate the positive charging, while these returning electrons are accounted for in the fluence of electrons back into the surface. The end result is that the fluence of electrons is limited by the capacitance of the underlying dielectric while, in principle, the fluence of photons is not limited by any surface process and depends only on the generation rate of photons in the SIW tens of microns within the surface.

The electron impact ionization source and electron density are shown in Fig. 5 at different times for the $\Delta h = 550$ μm surface modulation. The electron density, electric field, ionization source negative charge and photoionization source are shown in Fig. 6 the $\Delta h = 550$ μm surface. Looking first at Fig. 5, as the SIW climbs the upward slope of the first ridge (t = 1.4 ns) the SIW

12

propagates as it would on a flat surface – by a peak in the electron impact ionization (up to 10^{24}/cm^3-s) sustained by charge separation in the head of the SIW and charging of the underlying dielectric. As the SIW approaches the apex of the surface (t = 1.7 ns), photoionization provides seed electrons at the apex where electric field enhancements occurs. The seed electrons are then avalanched as a bulk IW across the valley to the next apex (t = 1.9 ns). The IW intersects the next ridge prior to the apex at a nearly normal angle of incidence due to the nearly normal electric field at the surface that results from polarization of the high permittivity surface. It is partly for this reason that the electron and photon fluences are maximum prior to the apex.

When the bulk IW strikes the surface, the surface locally charges negatively, which launches a SIW vertically downwards into the valley (t = 2.2 ns). This propagation of the SIW into the valley is aided by the vacuum electric field having a component parallel to the surface. This SIW proceeds along the surface to the nadir (bottom) of the valley, at which point it terminates. This termination in large part results from the voltage being shielded from the valley by the prior charging of the dielectric (t = 2.8 ns). The surface charging at the nadir is insufficient to produce an electric field component that would enable propagation in a direction that is opposite that of the applied electric field. For largely the same reasons (surface charging enabling an electric field component along the surface), a reverse SIW is launched from the apex of the first ridge (t = 2.2 ns).

This sequence of photoionization seeding a bulk IW wave launched from the apex, surface charging and SIW launched into valley is repeated for the second and third ridges. The third apex launches a bulk IW that is directed towards the electric field enhancement at the corner leading to the flat surface after the waves (t = 4.0 ns). The IW propagates over the valley. However, charging of the surface and corner does eventually produce a large enough component of the electric field parallel to the surface to launch a SIW into the third valley.

The steps leading to the launching of the IW from the first apex of the modulation are shown by the electron density, electric field, electron impact ionization source, negative charge and photo-ionization source in Fig. 6. Here, we see the propagation of the SIW up the slope of the first apex, launching of the bulk IW from the apex, and the landing of the bulk IW on the leading slope of the second apex. As the SIW propagates along the surface, the surface is charged negatively, with a reduction in electric field above the surface and an increase in electric field below the surface. This results in shielding of potential from the second and third apexes, which

13

contributes to the slowing of the SIW. At the time that a bulk IW is launched from the second apex, there are 4 distinct ionization waves in progress: 1) a bulk negative IW from the second to third apex, 2) a reverse bulk positive IW from the second to first apex, 3) a negative SIW propagating down the leading slope of the second apex and 4) a reverse positive SIW propagating down the leading slope of the first apex.

These propagation properties are, in part, dependent on the local capacitance (F/cm^2) of the dielectric. Larger capacitance generally corresponds to slower propagation of the SIW. The capacitance of the flat surface is 30 pF/cm^2. The average capacitance of the apex for $\Delta h = 500$ μm, based on adding a dielectric cone on top of the flat surface, is about 23 pF/cm^2. The average capacitance of the valley is about 90 pF/cm^2. There will be some speedup and slowdown of the SIW based on topology that produces a variation in capacitance.

The electron densities are shown in Fig. 7 for the ridges having amplitude $\Delta h = 400$ μm for voltage of – 6 kV to -16 kV. The pattern of the SIW launching a bulk IW from the apexes, charging the surface and launching SIWs through the valleys is nearly the same as the amplitude of the voltage is increased. The differences in SIW properties for different voltages are nominally in the propagation speed and maximum electron density. At -6 kV, the time required to cross the ridges (from initial upward slope to landing on the flat surface after the third apex) is 9.0 ns. For -16 kV, the time to cross the ridges is 1.0 ns. The maximum electron density at the first apex increases from 2×10^{14} cm^{-3} at -6 kV to 4×10^{15} cm^{-3} at -16 kV.

The electron density along the wavy surface for a positive SIW, with anode voltage of +12 kV, is shown in Fig. 8. Compared to the negative SIW, the positive SIWs are far more conformal to the surface. For even the large modulation $\Delta h = 550$ μm, there is some direct plasma coverage of the entire surface. With the positive SIW, electron fluxes are directed away from the surface while fluxes of different ions vary with mobility. We therefore show VUV fluences to the surface as an indication of plasma surface coverage in Fig. 9. The positions of the fluences for surfaces having different Δh are normalized by distance along the surface from the beginning to the end of the waves. With increasing Δh the modulation in the VUV fluence increases, however the amount of modulation is significantly less than for the negative SIW. All surfaces are directly covered by plasma up to $\Delta h = 550$ μm.

In general, the propagation of the positive SIW across the nonplanar surface is slower than for the negative SIW. This is in contrast to bulk ionization waves and SIWs on flat surfaces where

14

the positive IW tends to propagate faster than the negative IW [36,37]. In the bulk gas, propagation of the negative IW depends largely on diffusion of electrons in the direction propagation, which produces a more distributed space charge region and lower E/N. For positive streamers, propagation depends on photoionization in front of the head of the streamer, intrinsically a more rapid process than electron drift, while the head of the positive streamer is more compact, producing a larger space-charge induced electric field. The propagation of SIWs rely on charging of the underlying dielectric, which for negative SIWs is performed by electrons and for positive SIWs is performed by ions. The larger mobility of electrons enables a more rapid charging of the dielectric and faster SIW. With positive SIWs being more conformal across undulating surfaces, whereas negative may hop across the undulations, the positive SIWs must traverse over more surface, and so appear slower.

The positive SIWs are more conformal due to their reliance on photoionization to propagate and their inability to propagating in the diverging electric fields at the apex of the ridges. For the positive SIW, the surface appears to be cathode-like with a space charge sheath which accelerates positive ions into the surface. This acceleration could contribute to the surface hugging. Although secondary electron emission does not greatly affect propagation speed, the secondary emission does result in ionization close to the surface (electrons accelerated by the cathode-fall-like sheath). These local sources of ionization could also contribute to the conformality, though the effect is not large.

The sequence of events leading to propagation of positive SIWs over the waves for Δh = 300 μm is shown in Fig. 10 for an applied voltage of +12 kV. The electron density, electron impact ionization source and photoionization source are shown while the positive SIW propagates along the first two ridges. The positive SIW propagates along the upward slope in a similar manner as the negative SIW. However, propagation of the SIW on the downward slope requires seeding by photoionization, which is essentially a line-of-sight process. The downward slope of the wavy surface is in the shadow of the VUV radiation produced by the SIW propagating on the upward slope. As a result, there is a delay in the initiation of the SIW on the downward slope. When the SIW approaches the apex and photoionization is no longer shadowed, then the SIW is launched on the downward slope of the ridge.

A similar situation occurs for the negative SIW – photoionization occurs for the negative SIW as well. However, the intrinsically higher mobility of electrons and drift in the direction of

15

propagation enables avalanche of negative SIWs in the diverging electric field at the apex of the ridges. For positive-SIWs, the inability to propagate in the diverging electrics fields at the apex results in the path of least resistance being down the slope. The shadowing of the photo-ionizing radiation becomes more critical as the height of the ridges increases. For the large Δh amplitude ridges, the positive SIW stalls for several ns on the upward slope as photoionization is shadowed and unable to seed the avalanche on the downward slope.

As with the negative SIWs, we found only a weak dependence of positive SIW propagation speed and conformality on secondary electron emission from the surface. The speed of propagation did generally increase with increased rates of secondary electron emission, however weakly. The propagation of a positive SIW is sustained by photoionization that occurs in front of the streamer head where the large E/N in the head of the streamer then avalanches these seed electrons. Secondary electrons from the surface are emitted into regions where the E/N is generally below the value in the streamer head. Electrons must drift towards the streamer head where the E/N is large to significantly affect propagation speed. The secondary electron emission increases the rate of positive charging of the surface, which does contribute to increasing propagation speed.

IV. SIWs Over Surfaces with Cut Pores

The propagation of SIWs over porous dielectrics were investigated for the geometry shown in Fig. 1c for two configurations. The first configuration is for pores that are cut by the surface, exposing the inside surface of the pore for pores have increasing depth. The second configuration is a pore completely below the surface with a small opening to the surface. For these simulations, the dielectric has $\varepsilon_r = 4$ and is 7 mm thick. Pores are separated by 830 μm with the center of the first pore 2.2 mm from the edge of the electrode.

Pores are generally randomly located in porous materials. When a porous material is cut to create a flat surface, pores are cut-through leaving openings that vary from shallow spherical bowls to spheres with small openings to the ambient. Similar to wavy surfaces, the exposed surfaces that are convex to the plasma polarize and produce electric field enhancement. This electric field enhancement typically occurs at the edges of the cut pores. The surfaces that are concave to the plasma, such as at the bottom of the pore, polarize and produce a decrease in local electric field. Plasma properties shown in Fig. 11 for negative SIWs propagating over the dielectric with cut pores having a full pore diameter of 285 μm. Cut pores have depths of $\Delta h = 0$ μm (flat surface),

16

50 μm, 150 μm and 250 μm. The voltage magnitude is -30 kV with a rise time of 10 ns. (The higher voltage, material properties and geometry produce a thicker SIW.) The electron densities are shown at 16.5 ns after crossing over 3 cut-pores. The electron impact ionization source is shown at 11.5 ns, approximately the time that the ionization wave reaches the edge of the cut pore. The electron density, electron impact ionization source and E/N are shown in Fig. 12 at different times for the first pore having a depth of $\Delta h = 250$ μm.

As with the wavy surfaces, the SIW is able to follow the contours of the surface for moderate depths of the cut-pores, $\Delta h = 50$ - 100 μm, filling the pores with electron density exceeding 10^{13} cm^{-3}. This conformality is consistent with the results of Wang et al. [29]. With increasing depth of the pore, the radius of curvature of the exposed edge of the pore decreases, which increases the polarization and produces larger electric field enhancement. The electric field enhancement produces a local maximum in ionization rate which, as with the wavy surfaces, launches a bulk IW which crosses the volume of the pore. This is a form of SIW hopping, occurring here for $\Delta h > 100$ μm. As shown in the inset for ionization source in Fig. 11, the hopping of the SIW has two components. The first is the electric field enhancement on the leading edge of the pore. The electric enhancement is large enough that a bulk ionization wave is launched, which detaches the SIW from the surface. The second component is the electric field enhancement on the trailing edge of the pore, which attracts the bulk IW into the edge. The end result is that the leading inner surface of the pore (facing to the right) becomes progressively less exposed to the plasma as the cut-pore is located deeper into the dielectric.

The detachment of SIW from the surface is more severe than for the wavy surface. This more severe detachment is due to the re-entrant nature of the surface of the pore. With the wavy surface, the tangent to the surface always has a component that is parallel to the direction of the applied electric field. For this reason, in principle, wavy surfaces can be fully exposed to the plasma with SIWs in the direction of the applied electric field. For deeply buried cut-pores, such as $\Delta h = 250$ μm in Fig. 11d, the tangent to the surface points in the opposite direction of the applied electric field. As a result, a reverse or backwards SIW is required to cover the surface.

The propagation of the SIW in the most deeply cut pore, $\Delta h = 250$ μm, is shown in Fig. 12. As the SIW approached the pore (t=11.0 ns), electric field enhancement at the leading and trailing edges of the pore produce ionization sources which launch a bulk IW across the open pore. This transition from a SIW to a bulk ionization wave leaves the leading surface of the pore (facing to

17

the right) unexposed to the plasma. The bulk IW strikes the trailing edge of the pore, which charges the surface. This surface charge produces two SIWs (t = 11.5 ns). The first, a forward SIW, continues to propagate along the top surface towards the next pore. The second, a reverse SIW, propagates along the inner surface of the pore in a cathode seeking direction (t = 12.5 ns). The reverse SIW eventually stalls approaching the upward leading surface of the pore (t = 13.5 ns). There is insufficient plasma density and insufficient E/N to produce the charge density required to sustain ionization in the leading edge of the reverse SIW.

In taking a cut through a porous material, there is some likelihood of cutting through the opening through two interconnected pores. This cut may leave a small opening of the pore to the plasma, the size of which may be commensurate with the Debye length of the plasma in the SIW passing over the pore. The electron density, photoionization source and electron impact ionization source are shown in Fig. 13 for a negative SIW (-30 kV, 10 ns risetime) passing over a pore with a 25 μm opening to the plasma. When the SIW on the top surface reaches the opening to the pore, the electron density in the SIW is 5-7 × 10^{13} cm^{-3} with an electron temperature of 5.7 eV, corresponding to a Debye length of about 2.5 μm. With the opening to the pore being larger than the Debye length, the plasma is able to flow into the pore (t = 10 ns). This propagation of the SIW into the pore is aided by photoionization resulting from VUV flux passing through the pore opening from the plasma on the top surface.

With the SIW on the top of the surface intersecting with the trailing edge of the opening of the pore, the surface charges, which launches a SIW along the inner surface of the pore (t = 10.7 ns). As this SIW propagates along the inner surface, differential charging occurs between the inner surface and the opening to the pore, a location where there is natural electric field enhancement due to the curvature of the edges. A bulk IW is then launched across the pore (t = 12.2 ns). With the bulk IW dissipating, the SIW continues along the inner circumference of the pore (t = 13.5 ns). The SIW propagates for another 3 ns before stalling upon approaching the upwards leading surface of the pore (facing to the right). Radiation from high lying states of N_2 produces photoionization that is commensurate with ionization by electron impact processes. This photoionization continues after the SIW has dissipated, sustaining the plasma in the pore. Maximum plasma densities in the pore are $0.5 - 1 \times 10^{14}$ cm^{-3}. To some degree, the plasma in the pore is an extension of the plasma on the top surface. With the opening of the pore being larger than the Debye length, plasma is

18

able to flow into the pore, a similar observation to Zhang and Bogaerts who investigated plasma penetration into vertically oriented channels [38].

The electron density, photoionization source and electron impact ionization source are shown in Fig. 14 for a positive SIW (30 kV, 10 ns risetime) passing over the same pore with a 25 μm opening to the plasma. (Note that the properties in the plasma on top of the surface are saturated in color in order to show detail in the pore.) The entry of the positive SIW into the pore occurs from the leading edge of the opening, a consequence of the positive SIW being more conformal to the surface than negative SIW (as with the wavy surfaces) and the plasma density along the top surface being larger (1×10^{15} cm^{-3}). The plasma density that flows into the pore (t = 9.3 ns) is high enough to sustain a bulk IW wave that is launched across the pore (t = 9.4 – 9.6 ns). A corresponding SIW is not produced due to lack of significant surface charging. The bulk SIW intersects with the bottom of the pore (t = 10.0 ns) and dissipates. The plasma density produced in the pore exceeds 10^{15} cm^{-3}, an extension of the plasma on the top surface.

The electron density, photoionization source and electron impact ionization source are shown in Fig. 15 for a negative SIW (-30 kV) passing over pore with a 4 μm opening to the plasma. The size of the opening to the pore is about the same as the Debye length. The plasma is not able to readily flow into the pore. Electrons do leak into the pore (t = 10.0 ns) but not as a flowing plasma. The density of the electrons leaking into the pore, 3×10^7 cm^{-3}, is below the ambipolar limit. As a result, the flow of electrons into the pore is mono-polar and the electron flux is not accompanied by a neutralizing flux of positive ions. With the electron flow being nearly mono-polar, the flux into the pore is technically not a flowing plasma.

Initial plasma formation in the pore is dominated by photoionization by VUV flux produced in the plasma on the top surface and propagating through the opening. This photoionization resulting from VUV flux passing through the pore opening is indicated by the triangular, shadowed photoionization source (t = 10.0 ns). At this time, the electron impact ionization source is essentially zero. This initial seeding of electrons in the pore by photoionization then leads to a bulk ionization wave through the volume of the pore that intersects with the inner surface of the pore. Upon charging the surface, there is a transition to a SIW (t = 10.6 ns). Once plasma penetrates into the pore, there are two components of photoionization. The first results from VUV flux that enters through the opening in the pore (shadowed, triangular shaped ionization source at t = 10.6 ns). The second source of photoionization produced by the plasma inside the pore (ionization

19

source that overlaps with the plasma density at t = 10.6 ns). The SIW continues to propagate along the inner surface (t = 12.6 – 16.6 ns) while there is continuous leakage of electrons from the plasma on the top surface into the pore. The electric field enhancement at the opening of the pore then launches these electrons into a weak bulk IW. The plasma density inside the pore does not exceed 5×10^{10} cm^{-3}.

Plasma properties for a positive SIW (30 kV) passing over a pore with a 4 μm opening are shown in Fig. 16. The local Debye length in the SIW on the top surface when arriving at the pore is about 1 μm, and so there is some direct flow of plasma into the pore through the 4 μm opening (t=9.3 ns) producing an electron density of (3×10^{12} cm^{-3}). This plasma density is produced in large part by flow into the pore and local electron impact ionization, and secondarily by photoionization. Again, there are two components to the photoionization – due to photons transmitted through the pore and photons produced inside the pore (t = 9.3 ns). In spite of there being sufficient charge density in the pore to generate a bulk IW, charging of the top surface of the dielectric shields potential from the pore, and reduces E/N near the pore opening where the electron density is large enough to launch an IW (t = 9.5 ns). Due to the low E/N, the ionization source transitions to being negative (t = 10.4 ns). Coupled with onset of free diffusion of electrons in the sub-ambipolar densities, the electron density rapidly decays (t = 13.0 ns).

V. Implications for Plasma Treatment of Droplets on Surfaces

With transmission of viral agents such as SARS-CoV-2 being dominantly through aerosols, there is increasing interest in atmospheric pressure plasma treatment of aerosol droplets and of virus containing droplets on surfaces for decontamination [39]. The interest here is in the plasma treatment of droplets on surfaces. There are several modes of such treatment, generally classified as direct and indirect. For direct treatment, the plasma is in contact with the surface and droplet. For indirect treatment, only the plume of plasma produced RONS (reactive oxygen and nitrogen species) treat the surface and droplet. As mentioned in the introduction, the majority of direct atmospheric pressure treatment of surfaces involves SIWs.

One of the advantages, or at least features, of direct treatment of surfaces is the large fluence of VUV radiation onto the surface that can be generated by the SIW. With the mean-free-path for absorption of the VUV produced by bulk IWs in air being only tens of microns, remote treatment of surfaces will generally not produce large fluences of VUV radiation onto the surface,

20

resulting in direct treatment being more effective [40]. Remote plasma jets sustained in rare gases producing a rare-gas dominated plume will produce larger fluences of VUV radiation onto surfaces. However, even these fluences are small compared to VUV fluences produced by direct treatment.

The mean-free-path for absorption of VUV radiation produced by air plasmas in water (photo-absorption cross section 2×10^{-17} cm^2 [41]) is about 15 nm. About 1/3 of this absorption results in ionization and 2/3 in neutral dissociation producing OH + H. Rapid reaction of H_2O^+ with water produces hydronium (H_3O^+) and OH. The end result is that absorption of three VUV photons produces on the average three OH radicals and H_3O^+ in this thin, 10-20 nm surface layer of the water. The OH, if not quickly reacting with organics, will produce biocidal H_2O_2 while the H_3O^+ contributes to acidification.

The propagation of negative and positive SIWs along surfaces having water droplets was investigated with the goal of assessing the best strategy for surface decontamination. The geometry is shown in Fig. 1b for a hemispherical water droplet ($\varepsilon_r = 80$) on the surface 475 μm in diameter. Since the simulation is 2-dimensional, the droplet appears to be a half-cylinder rod oriented perpendicular to the computational domain. The electron density and electron impact ionization source as a negative SIW approaches and propagates over the droplet are shown in Fig. 17. The general behavior is similar to that of a negative SIW propagating along the wavy dielectric surface and the surface having cut-pores. The SIW intersects the droplet (1.5 ns) and propagates along the ascending slope (2.2 ns). Upon reaching the apex of the droplet where there is electric field enhancement resulting from polarization of the droplet, the SIW separates from the droplet and launches a bulk IW (2.5 ns). This detachment of the SIW leaves the right face of the droplet untouched by plasma.

The bulk IW is redirected towards the surface by the applied electric field, intersecting the surface about 300 μm from the right edge of the droplet (2.5 ns). The charging of the dielectric at that intersection launches two SIWs. The SIW propagating to the right away from the droplet is negative (2.7 ns). The SIW propagating to the left towards the droplet is positive. This positive SIW intersects with the droplet and continues to propagate up the surface of the droplet before stalling (2.8 ns). On these timescales (shorter than the dielectric relaxation time of water) the surface of the water also charges. This surface charging also launches a positive SIW from the apex of the droplet down the leading slope of the droplet (facing left).

21

The electron density and electron impact ionization source for a positive SIW propagating over the hemispherical droplet is shown in Fig. 18. Similar to the positive SIW propagating along the wavy surface, the SIW is essentially conformal to the surface of the droplet with there being some small detachment on the trailing edge of the droplet (facing right). The electron impact ionization source follows the contours of the droplet until reaching the dielectric surface on the right side of the droplet, at which time the SIW continues to propagate along the dielectric as a conventional SIW.

In their simulations of positive SIWs propagating over indentations in dielectric surfaces, Wang et al [29] found that the radius of the streamer head varies over the surface as various structures are traversed. We observe similar dependencies for positive SIWs, though we have not found a quantitative correlation between surface properties and radius of the streamer head. For example, the radius of the streamer head, as indicated by the electron impact ionization in Fig. 18, is smaller as the SIW ascends the droplet than when descending the droplet. The general correlation is that as the SIW begins to detach from the surface, the radius of the streamer head increases, an observation that extends to negative SIWs.

The fluences of VUV photons onto the surface of the droplet are shown in Fig. 19 for the negative and positive SIWs. The fluence of VUV radiation resulting from the positive SIW covers the entire surface of the droplet, albeit with a decreasing magnitude from the leading edge to the trailing edge of the droplet. The fluence of VUV radiation result from the negative SIW decreases by nearly 3 orders magnitude from the leading to the trailing edge of the droplet – a result of the detachment of the SIW from the droplet. The increase in VUV fluence at the trailing edge of the droplet exclusively results from the reverse positive SIW that is launched by the charging of the dielectric where the bulk IW wave strikes. When assessing the VUV fluence onto the droplet, we recommend discounting the fluence produced the reverse SIW since this is case specific. Discounting the VUV exposure due to the reverse SIW, the side of the droplet facing to the right is not exposed to the VUV radiation.

With VUV fluences of 10^{14} cm^{-2}, the surface layer of the water droplet would be acidified by formation of H_3O^+ to a pH < 1-2, and in the process forming a concentration of 18 M (moles/liter) of solvated electrons. Assuming the OH radicals produced by VUV photolysis dominantly produce H_2O_2, the concentration of H_2O_2 in the surface layer would be an extraordinarily high 50 M. Averaged over the surface of the droplet, these concentrations will be 2-3 times smaller for

22

negative SIWs compared to positive-SIWs. These concentrations and acidity are in thin layers at the surface of the droplet. That said, these species do then diffuse into the bulk of the droplet, and with repetitive pulsing. These results suggest that positive SIWs would be more effective at activating surface resident droplets than negative SIWs.

VI. Concluding Remarks

Atmospheric pressure plasmas interacting with dielectric surfaces usually transition into some form of surface ionization wave (SIW). In this paper, results from a computational investigation of SIWs sustained in humid air propagating over wavy dielectrics, cut-pores and droplets were discussed. The period (300 μm) and height (flat to $\Delta h = 550$ μm) of the wavy surface are commensurate with the thickness of the SIW (up to 100-200 μm). Due to polarization in the applied electric field, enhancement of the electric field occurs at locations along the surface having small radii of curvature. For these conditions, the electric field enhancement occurs at the apex of the waves.

We found that negative SIWs were able to adhere to wavy surfaces having only moderate amplitudes, $\Delta h < 100$ - 150 μm. For larger amplitudes, the negative SIW detaches from the surface near the apex of the wavy surface, and becomes a bulk ionization wave (IW). The bulk IW propagates back onto the surface, charging the surface, and launching SIWs – negative in the forward direction and positive in the backwards direction. This hopping of the SIW results in non-uniform exposure of the surface by the SIW. Positive SIWs are more able to adhere to the wavy surface, producing more uniform exposure of the surface to ions and VUV radiation. However even positive SIWs are ultimately limited in their propagation across wavy surfaces by shadowing of the photoionization required to sustain the SIW.

These trends extend to SIWs propagating across the non-planar surfaces of porous materials which cut through and expose open pores. Negative SIWs are able to adhere to the surfaces f shallow open pores. However, the electric field enhancement at the edges of the cuts through deeper pores will launch bulk IWs that hop or skip over the pores. Although there is some backwards propagation of SIWs inside the pore, there are generally surfaces that are left unexposed to the plasma for both negative and positive SIWs.

In the limit of buried pores with small openings to the plasma, the filling of the pores depends on the size of the openings compared to the local Debye length when the SIW arrives at the

opening. If the opening is larger than the Debye length, plasma flows into the pore from the SIW. The dynamics of the plasma inside the pore can be complex, resulting in the inside surfaces generally not being uniformly exposed to the plasma. With the opening to the pore being commensurate or smaller than the local Debye length, plasma will not directly flow into the pore. Diffusion of electrons into the pore as a non-neutral current may occur. Photo-ionization by VUV photons generated outside the pore and propagating through the opening also produces electrons in the pore. Neither sources are typically sufficient to sustain a large plasma density in the pore.

These trends imply that more uniform treatment of non-planar surfaces by SIWs will most likely occur by positive waves provided that shadowing of photoionizing radiation produced in the head of the SIW is not too severe. This is particularly relevant to the direct plasma treatment of water droplets on surfaces, a material with a large permittivity which is highly polarized by the applied electric field, thereby producing electric field enhancement at its surface. Negative SIWs will most hop over droplets leaving portions of the surface of the droplet unexposed. Positive SIWs being more conformal to the surface produce more uniform exposure of the droplet.

Conflict of Interest

The authors have no conflicts of interest to disclose.

Data Availability

The data that support the findings of this study are available from the corresponding author upon reasonable request.

References

1. V. I. Gibalov and G. J. Pietsch, Plasma Source Sci. Technol. **21**, 024010 (2012).

2. X. Li, A. Sun, G. Zhang and J. Teunissen, Plasma Source Sci. Technol. **29**, 024010 (2020).

3. H. Hoft, M. Kettlitz, M. M. Becker, T. Hoder, J. Phys. D **47**, 465206 (2014).

4. X. Xu, Thin Solid Films **390,** 237 (2001).

5. A. V. Likhanskii, M. N. Shneider, S. O. Macheret and R. B. Miles, J. Appl. Phys. **103,** 053305 (2008).

6. S. A. Stepanyan, A. Yu. Starikovskiy, N. A. Popov and S. M. Starikovskaia, Plasma Source Sci. Technol. **23**, 045003 (2014).

7. C. Nau-Hix, T. M. Holsen and S. Mededovic Thagard, Plasma Proc. Polym. e220036 (2022).

8. S. A. Shcherbanev, Ch. Ding, S. M. Starikovskaia and N. A. Popov, Plasma Source Sci. Technol. **28**, 065013 (2019).

9. M. Florkowski, Measurement **186**, 110170 (2021).

10. F. Pechereau, Z. Bonaventura and A. Bourdon, Plasma Source Sci. Technol. **25**, 044004 (2016).

11. P. Viegas, E. Slikboer, Z. Bonaventura, E. Garcia-Caurel, O. Guaitella, A. Sobota and A. Bourdon, Sci. Report **12**, 1181 (2022).

12. B. Huang, C. Zhang, I. Adamovich, Y. Akishev and Tao Shao, Plasma Sources Sci. Technol. **29**, 044001 (2020).

13. P. Viegas, E. Slikboer, Z. Bonaventura, O. Guaitella, A. Sobota and A. Bourdon, Plasma Sources Sci. Technol. **31**, 053001 (2022).

14. E. Slikboer, P. Viegas, Z. Bonaventura, E. Garcia-Caurel , A. Sobota , A. Bourdon and O. Guaitella, Plasma Sources Sci. Technol. **28** 095016 (2019).

15. R. Joshi, J. F. Kolb, S. Xioa and K. H. Schoenbach, Plasma Proc. Polym. **6**, 763 (2009).

16. X. Li, A. Sun, Guanjun Zhang and J. Teunissen, Plasma Sources Sci. Technol. **29**, 065004 (2020).

17. H. K. Meyer, F. Mauseth, R. Marskar, A. Pedersen and A. Blaszczyk, Trans. Diel. Elect. Insul. **26**, 1163 (2019).

18. H. K. H. Meyer, R. Marskar, H. Gjemdal and F. Mauseth, Plasma Source Sci. Technol. **29**, 115015 (2020).

19. X. Li, A. Sun and J. Teunissen, Trans. Diel. Elect. Ins. **27**, 1178 (2020).

20. F. Pechereau, J. Jansky and A. Bourdon, Plasma Source Sci. Technol. **21**, 055011 (2012).

21. M. Kettlitz, R. Klink, H. Hoft and R. Brandenburg, Eur. Phys. J. D **74**, 110 (2020).

22. T. Hoder, H. Hoft, M. Kettiltz, K-D. Weltmann and R. Brandenburg, Phys. Plasma **19**, 070701 (2012).

23. W. Ning, D. Dai and L. Li, Plasma Source Sci. Technol. **27**, 08LT01 (2018).

24. Q. Wang, W. Ning, D. Dai and Y. Zhang, Plasma Proc. Polym. **17**, e1900182 (2020).

25. S. Jahanbakhsh, V. Bruser and R. Brandenburg, Plasma Sources Sci. Technol. **27**, 115011 (2018).

26. Z. Mujahid and J. Schulze, AIP Advances **12**, 01528 (2022).

25

27. Z. Mujahid, J. Kruszelnicki, A. Hala and M. J. Kushner, Chem. Engr. J. **382**, 123038 (2020).

28. Y. Sun, B. Zhang, C. Wang and G. Zhang, Adv. Electron. Mater. **7**, 2100369 (2021).

29. F. Wang, L. Wang, S. Chen, Q. Sun and L. Zhong, Trans. Diel. Elect. Insul. **28**, 2186 (2021).

30. S. A. Norberg, E. Johnsen and M. J. Kushner, Plasma Source Sci. Technol. **24**, 035206 (2015).

31. J. Kruszelnicki, K. W. Engeling, J. E. Foster and M. J. Kushner, J. Phys. D: Appl. Phys. **54**, 104001 (2021).

32. A. M. Lietz and M. J. Kushner, J. Phys. D: Appl. Phys. **49**, 425204 (2016).

33. B. M. Goldberg, P. S. Bohm, W. Czarnetzki, I. V. Adamovich and W. R. Lempert, Plasma Source Sci. **24**, 055017 (2015).

34. V. Petrishchev, S. Leonov and I. V. Adamovich, Plasma Source Sci. **23**, 065002 (2014).

35. B. Huang, C. Zhang, I. Adavmovich, Y. Akishev and T. Shao, Plasma Source Sci. Technol. **29**, 044001 (2020).

36. N. Yu Babaeva and G. V. Naidis, Trans. Plasma Sci. **25**, 375 (1997).

37. A. Luque, V. Ratushnaya and U. Ebert, J. Phys. D: Appl. Phys. **41**, 234005 (2008).

38. Q-Z. Zhang and A. Bogaerts, Plasma Source Sci. Technol. **27**, 035009 (2018).

39. H. Gao, G. Wang, B. Chen, Y. Zhang, D. Liu, X. Lu, G. He and K. Ostrikov, Plasma Source Sci. Technol. **30,** 053001 (2021).

40. R. Brandenburg, H. Lange, T. von Woedtke, M. Stieber, E. Kindel, J. Ehlbeck and K-D. Weltman, Trans. Plasma Sci. **37**, 877 (2009).

41. D. H. Katayama, R. E. Huffman and C. L. O'Bryan, J. Chem. Phys. **59**, 4309 (1973).

26

Figure Captions

1. Schematics of the computation domains. a) Geometry for the investigation of SIWs propagating over wave surfaces. b) Location of water droplet. c) Configurations of (left) cut pore and (right) buried pore with a small opening to the plasma.

2. Properties of a negative SIW propagating across a flat dielectric surface with relative permittivity $\varepsilon_r = 10$. a) Electron density, b) electron impact ionization source, c) electron temperature, d) electric field (with arrows showing the direction of the electric field) and e) photoionization source. The range of values in the image are noted in the frame, with the number of decades for log-plots.

3. Electron density for negative SIWs propagating over wavy surfaces of different valley-to-crest heights, Δh. a) $\Delta h = 0$ μm (flat), b) 50 μm, c) 100 μm, d) 200, e) 400 μm and f) 550 μm. The range of values plotted are 1×10^{13} to 3×10^{15} on a logscale at times indicated in each frame. The plasma detaches from the surface for wavy surfaces having $\Delta h > 150$ μm.

4. Fluences of electrons and VUV photons onto the wavy surface by a negative SIW for different valley-to-crest heights, Δh. a) $\Delta h = 50$ μm, b) 100 μm, and c) 400 μm. The position coordinate is measured along the wavy surface. the locations of the crests of the waves are noted by the insets and the dashed vertical lines. With increasing Δh, the fluence across the surface becomes less uniform, with surfaces at large heights receiving no exposure.

5. Propagation of the negative SIW across the wavy surface having a valley-to-crest height of $\Delta h = 550$ μm for (left column) electron impact ionization source and (right column) electron density. The time sequence is down each column. The range of values plotted for each quantity are indicated in the top row., with the number decades for log plots.

6. Propagation of the negative SIW across the wavy surface having a valley-to-crest height of $\Delta h = 550$ μm. a) Electron density, b) electric field, c) electron impact ionization source, d) negative charge density and e) photoionization source. The times for the columns are (left to right0 1.5 ns, 1.8 ns and 2.1 ns. The range of values plotted in each image are indicated in each frame, with the number decades for log plots.

7. Electron density during propagation of the negative SIW across the wavy surface having a valley-to-crest height of $\Delta h = 400$ μm for cathode voltage of a) -6 kV, b) -8 kV, c) -12 kV and d) -16 kV. The time for each image and range of values plotted on a 3-decade log scale are
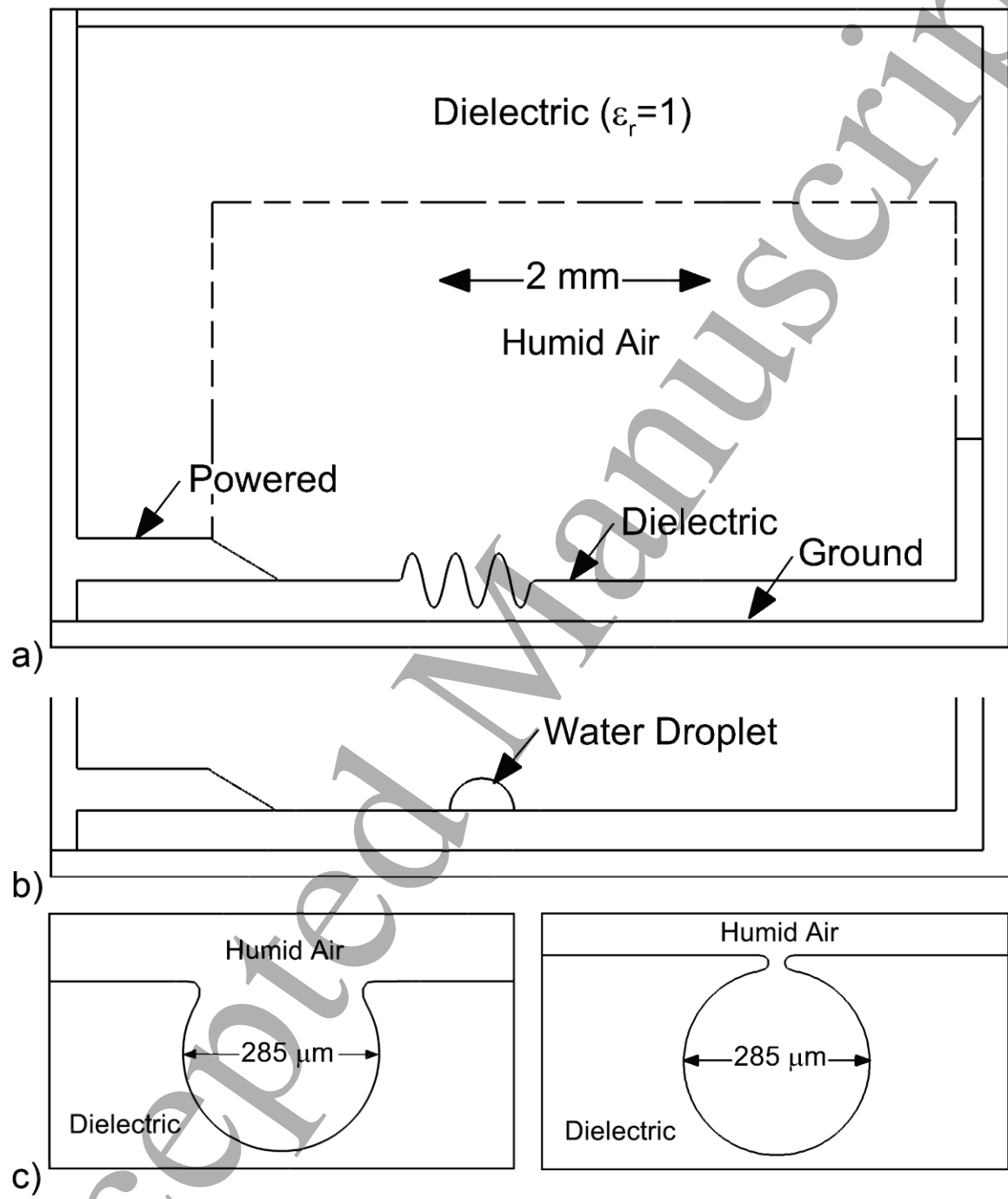
27

indicated in each frame.

8. Electron density for positive SIWs propagating over wavy surfaces of different valley-to-crest heights, Δh. a) $\Delta h = 0$ μm (flat), b) 50 μm, c) 100 μm, d) 200, e) 400 μm and f) 550 μm. The range of values plotted are 1×10^{12} to 3×10^{15} cm^{-3} on a logscale at times indicated in each frame. The plasma generally adheres to the surface for all wave heights.

9. Fluences VUV photons onto the wavy surface by a positive SIW for different valley-to-crest heights, $\Delta h = 50$ μm to 550 μm. The position coordinate is measured along the wavy surface. The locations of the crests of the waves are noted by the insets and the dashed vertical lines. With increasing Δh, the fluence across the surface becomes less uniform, but coverage is maintained.

10. Propagation of the positive SIW across the wavy surface having a valley-to-crest height of $\Delta h = 200$ μm. a) Electron density, b) electron impact ionization source, and c) photoionization source. The times for the columns are (left to right0 1.5 ns, 1.8 ns and 2.1 ns. The range of values plotted in each image are indicated in each frame, with the number decades for log plots.

11. Propagation of a negative SIW across a surface with cut pores with diameter 285 having different depths of the pores, Δh. a) $\Delta h = 0$ μm (flat), b) 50 μm, c) 150 μm and d) 250 μm. Electron density (maximum 5×10^{13} cm^{-3}, 2-decade log scale) is shown in the left column at 16.5 ns after the SIW crosses the 3 cut pores. Electron impact ionization source (maximum 5×10^{22} cm^{-3}s^{-1}, 3 decade log scale) is shown in the right column for the first (left-most) pore when the SIW arrives at 11.5 ns.

12. Plasma properties for the negative SIW arriving at the first, left-most cut-pore (diameter 285 μm) having depth $\Delta h = 250$ μm at times of a) 11.0 ns, b) 11.5 ns, c) 12.5 ns and d) 13.5 ns. The columns (left to right) show electron density, electron impact ionization source and E/N. The range of values for each quantity (and number of decades for log-plots) are shown at the top of each column.

13. Plasma properties for the negative SIW arriving at the first, left-most buried pore (diameter 285 μm) having an opening to the plasma of 25 μm at times of a) 10.0 ns, b) 10.7 ns, c) 12.2 ns and d) 13.5 ns. The columns (left to right) show electron density, photoionization source and electron impact ionization source. The range of values for each quantity (4-decade log scale) are shown at the top of each column. Values in the bulk plasma on top of the surface
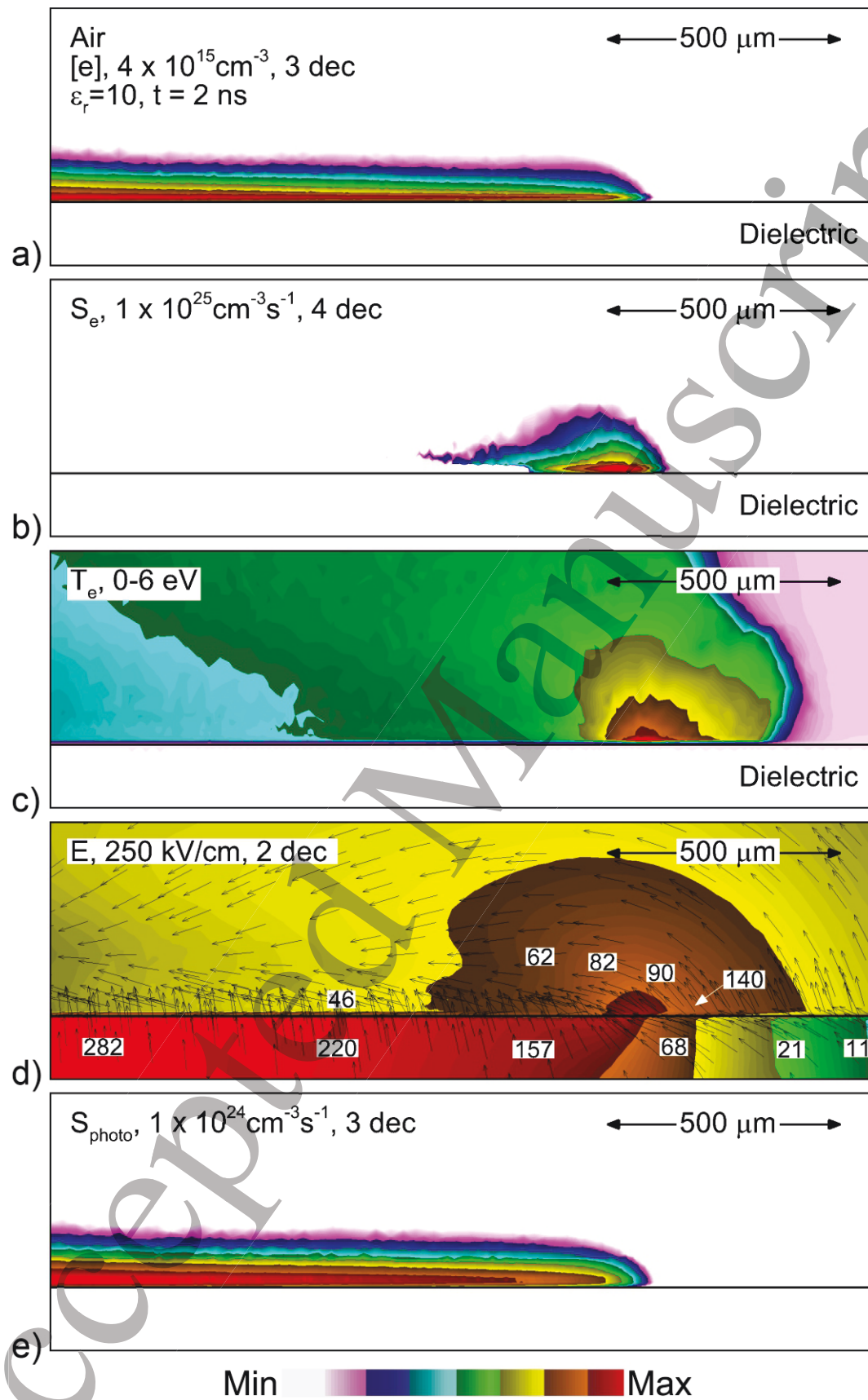
28

may be saturated for the range of values in the image. The range of values was chosen to emphasize the in-pore properties.
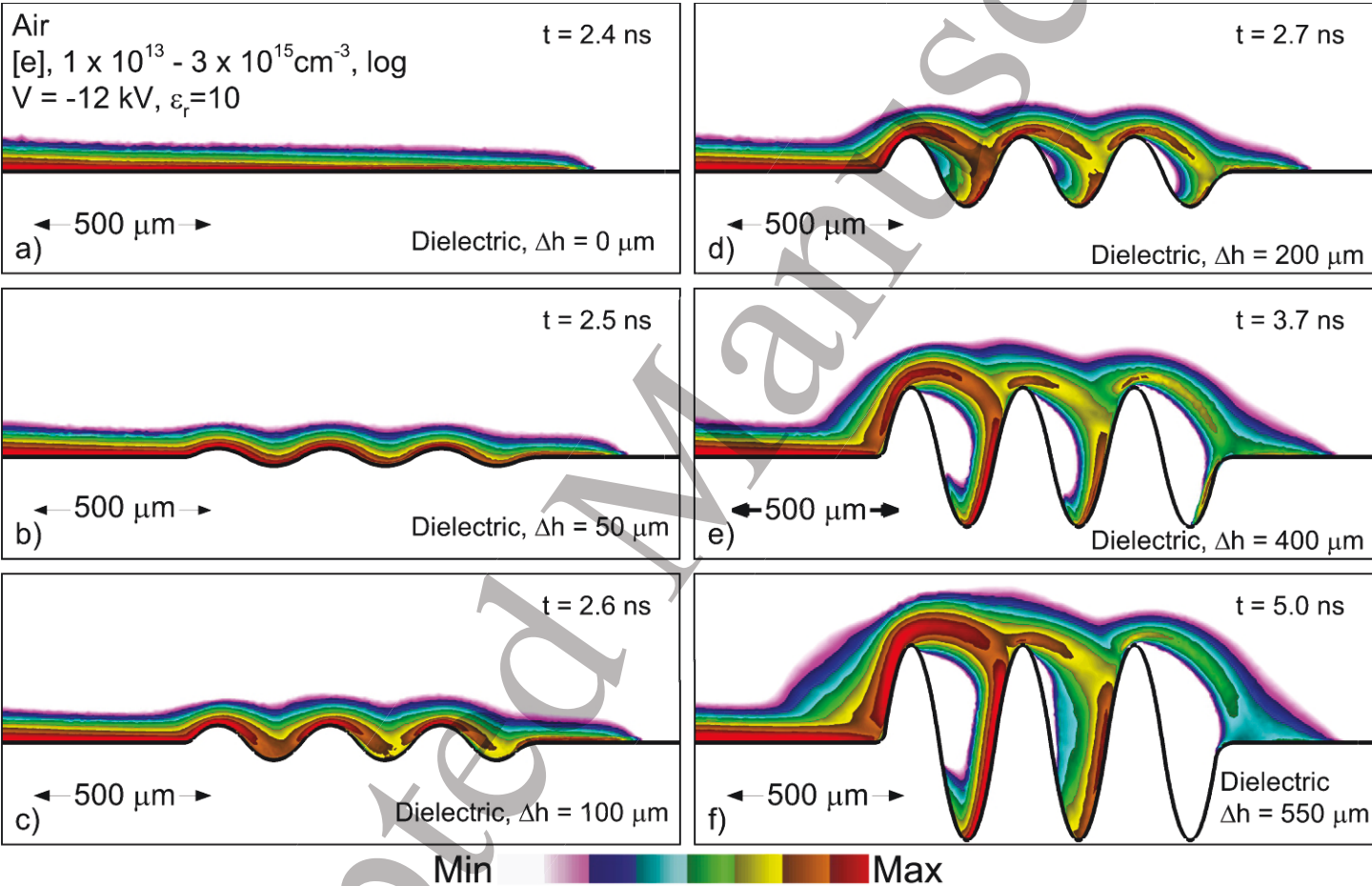
14. Plasma properties for the positive SIW arriving at the first, left-most buried pore (diameter 285 μm) having an opening to the plasma of 25 μm at times of a) 9.3 ns, b) 9.4 ns, c) 9.6 ns and d) 10.0 ns. The columns (left to right) show electron density, photoionization source and electron impact ionization source. The range of values for each quantity and number of decades for these log plots are shown at the top of each column. Values in the bulk plasma on top of the surface may be saturated for the range of values in the image. The range of values was chosen to emphasize the in-pore properties.

15. Plasma properties for the negative SIW arriving at the first, left-most buried pore (diameter 285 μm) having an opening to the plasma of 4 μm at times of a) 10.0 ns, b) 10.6 ns, c) 12.6 ns and d) 16.6 ns. The columns (left to right) show electron density, photoionization source and electron impact ionization source. The number of decades for these log plots are shown at the top of each column. The maximum values for each image are shown in the frame. Values in the bulk plasma on top of the surface may be saturated for the range of values in the image. The range of values was chosen to emphasize the in-pore properties.

16. Plasma properties for the positive SIW arriving at the first, left-most buried pore (diameter 285 μm) having an opening to the plasma of 4 μm at times of a) 9.3 ns, b) 9.5 ns, c) 10.4 ns and d) 13.0 ns. The columns (left to right) show electron density, photoionization source and electron impact ionization source. The number of decades for these log plots are shown at the top of each column. The maximum values for each image are shown in the frame. Values in the bulk plasma on top of the surface may be saturated for the range of values in the image. The range of values was chosen to emphasize the in-pore properties.

17. Plasma properties of a negative SIW propagating over a water droplet (475 μm in diameter) on a flat dielectric for different times (down each column). a) Electron density and b) electron impact ionization source. The maximum value and number of decades for these log plots are shown in the top frame. The negative SIW detaches from the surface due to electric field enhancement by the polarized droplet.

18. Plasma properties of a positive SIW propagating over a water droplet (475 μm in diameter) on a flat dielectric for different times (down each column). a) Electron density and b) electron impact ionization source. The maximum value and number of decades for these log plots are
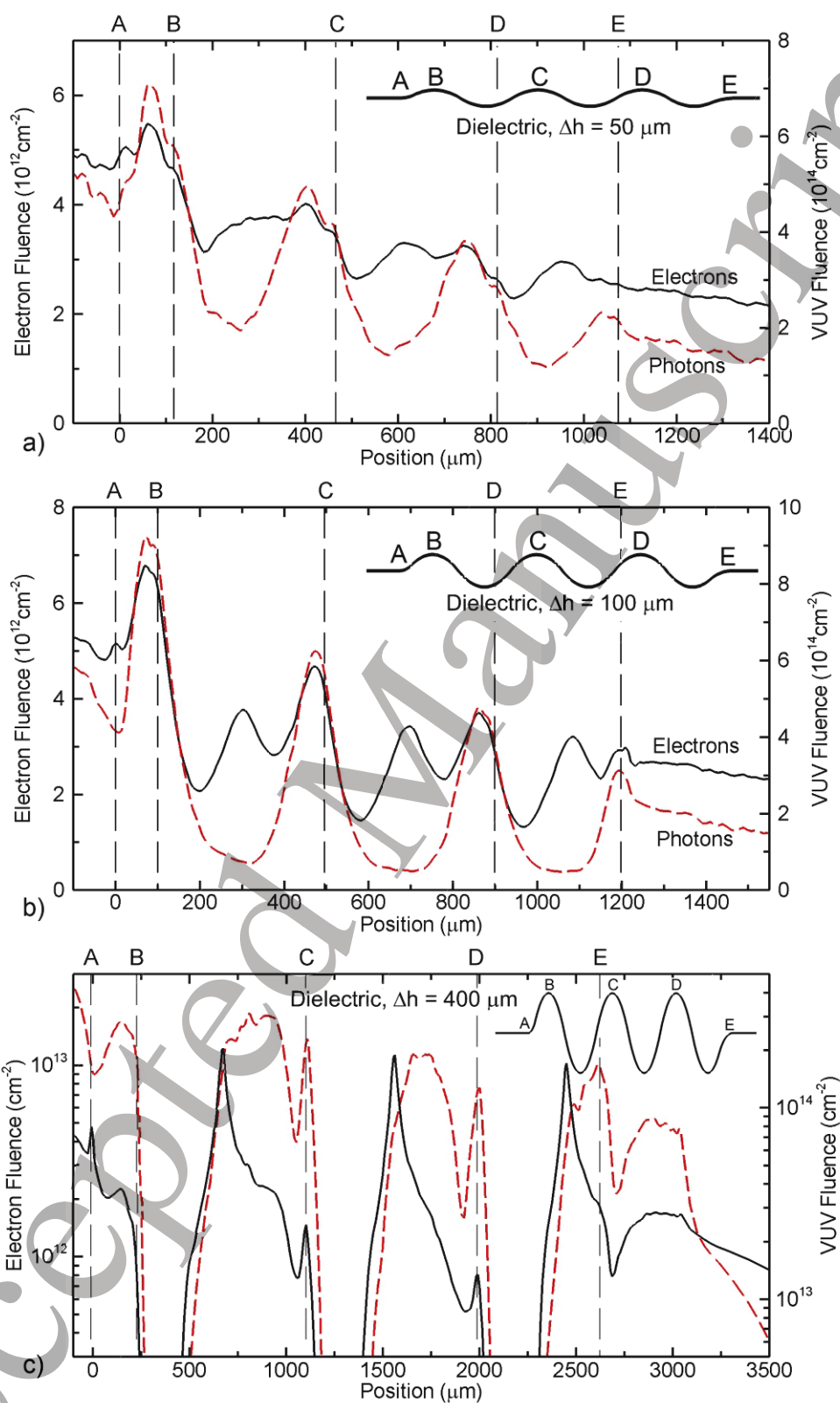
shown in the top frame. The negative SIW adheres to the surface of the droplet.
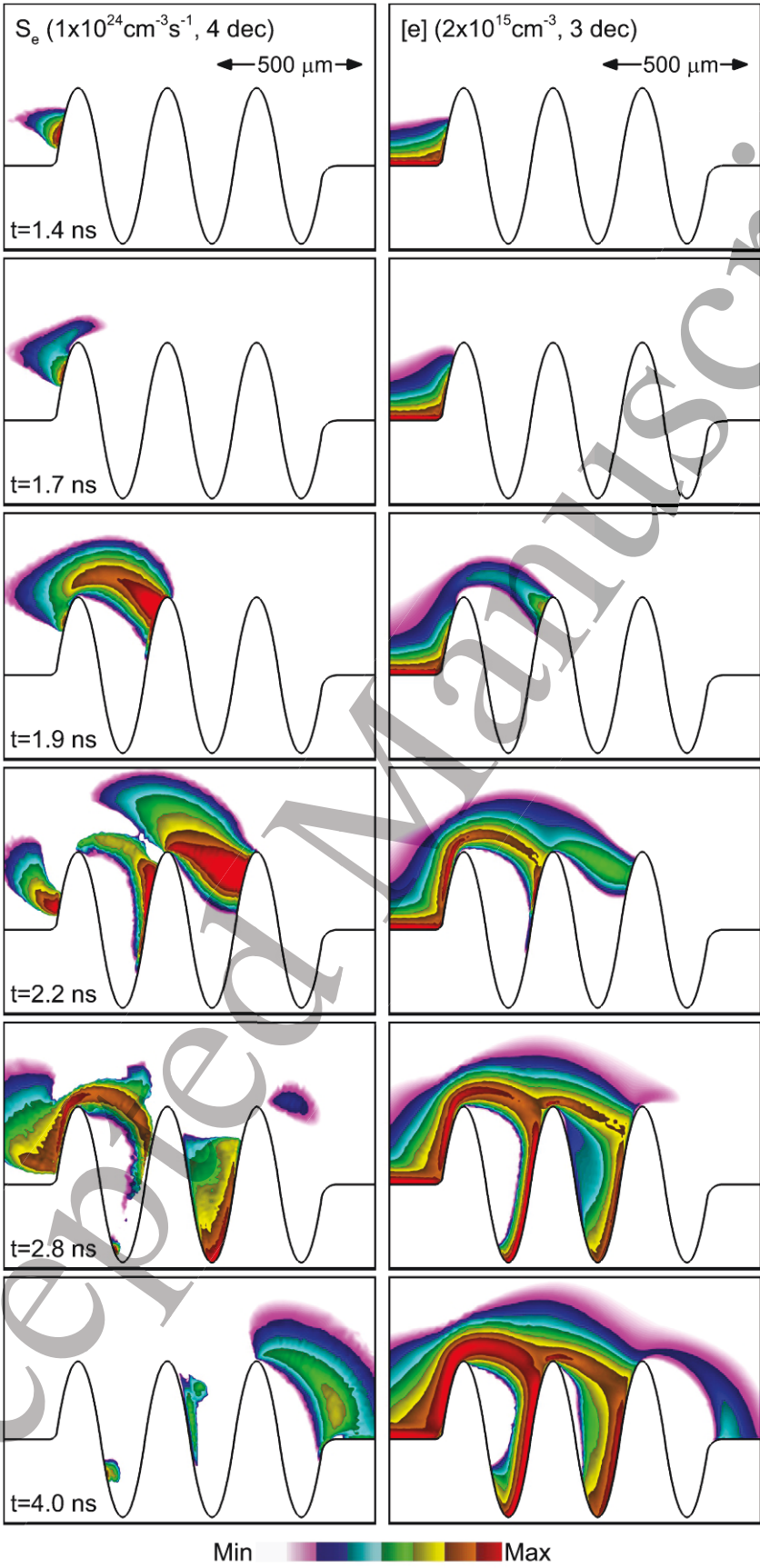
19. VUV fluence onto the surface of the water droplet by negative and positive SIW as a function of position on the surface. A and B are the leading and trailing edges of the droplet. The rebound at position > 600 μ in the fluence for the negative SIW is due to due a reverse wave that returns to the droplet, which is likely case specific.
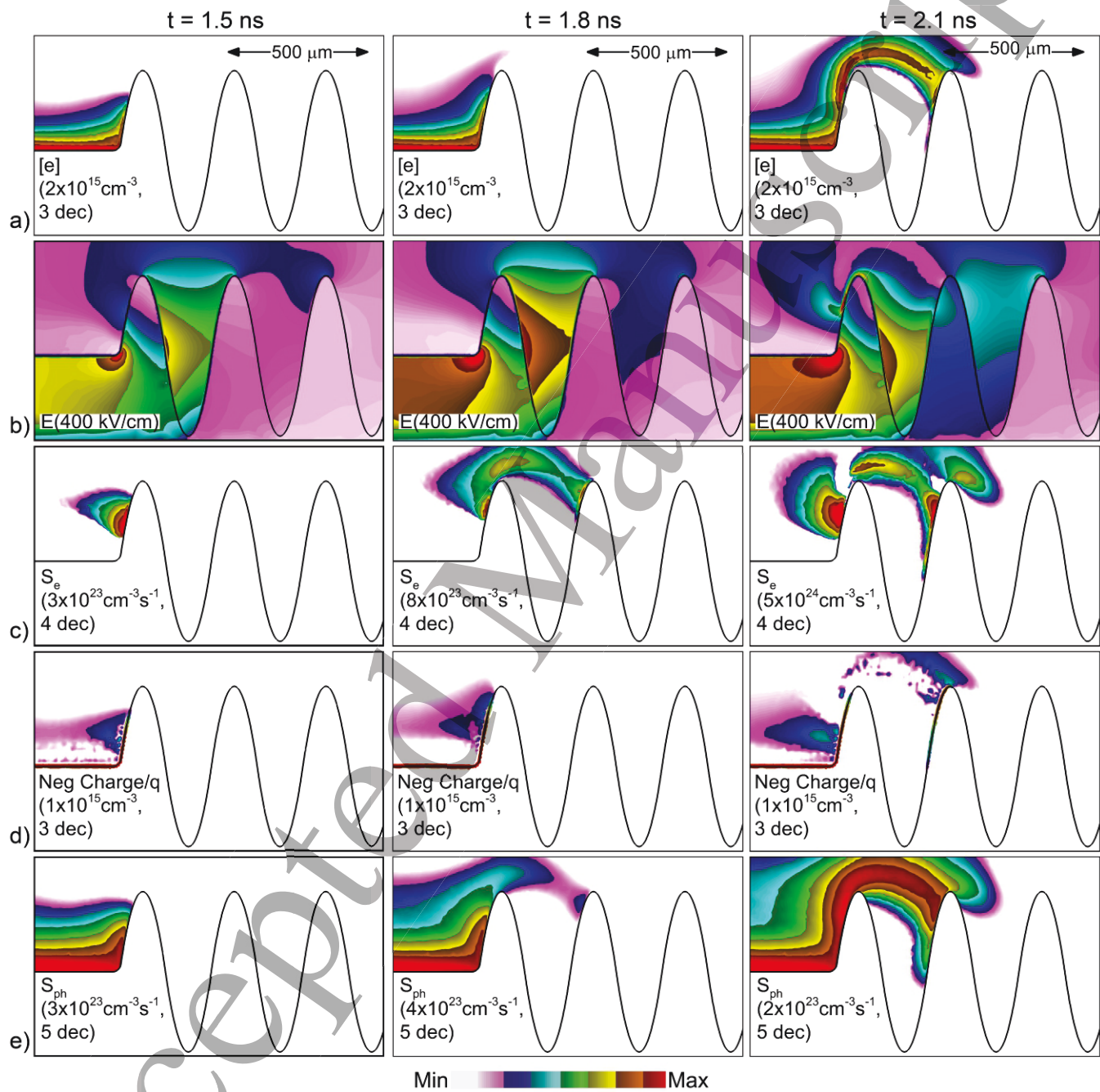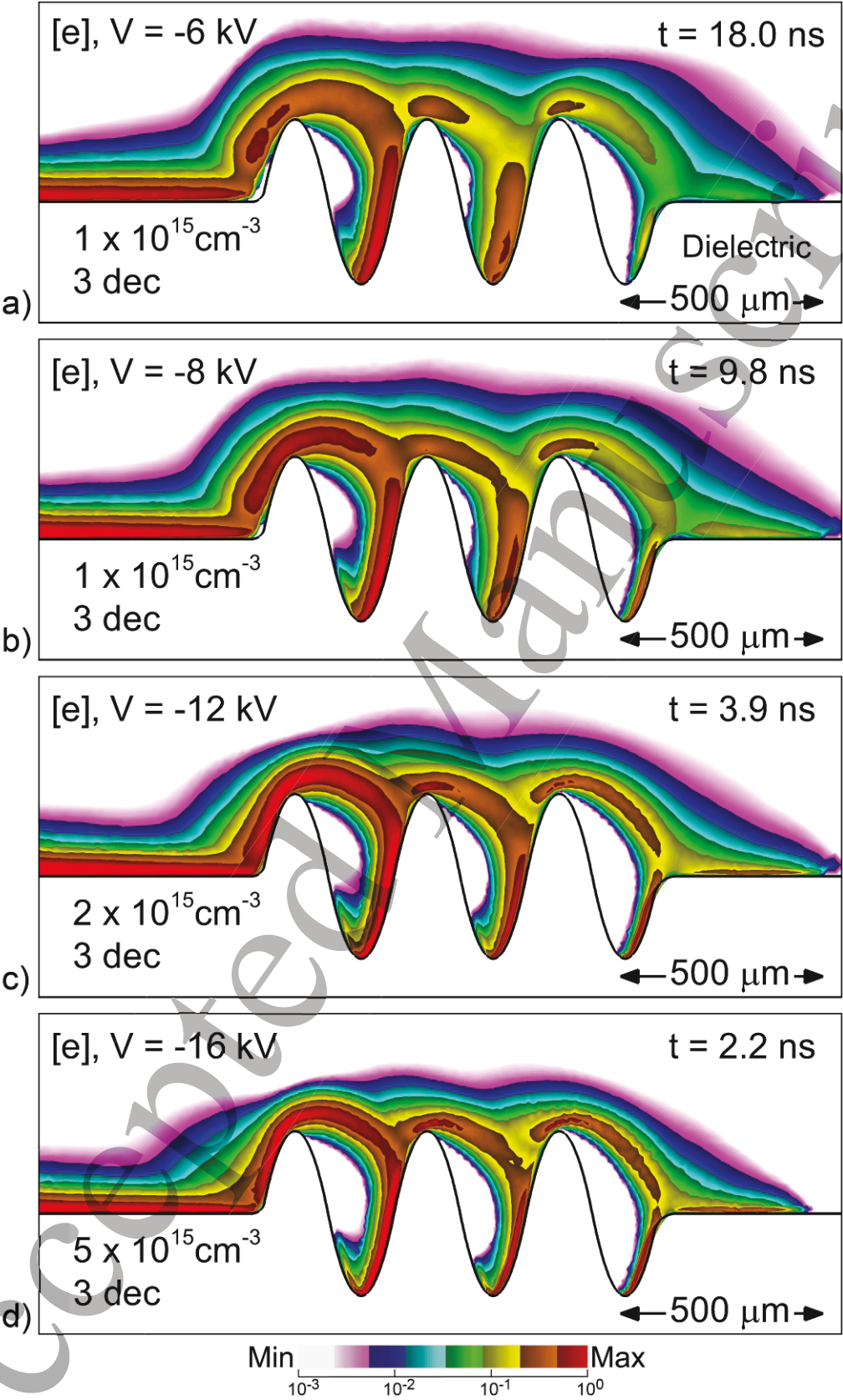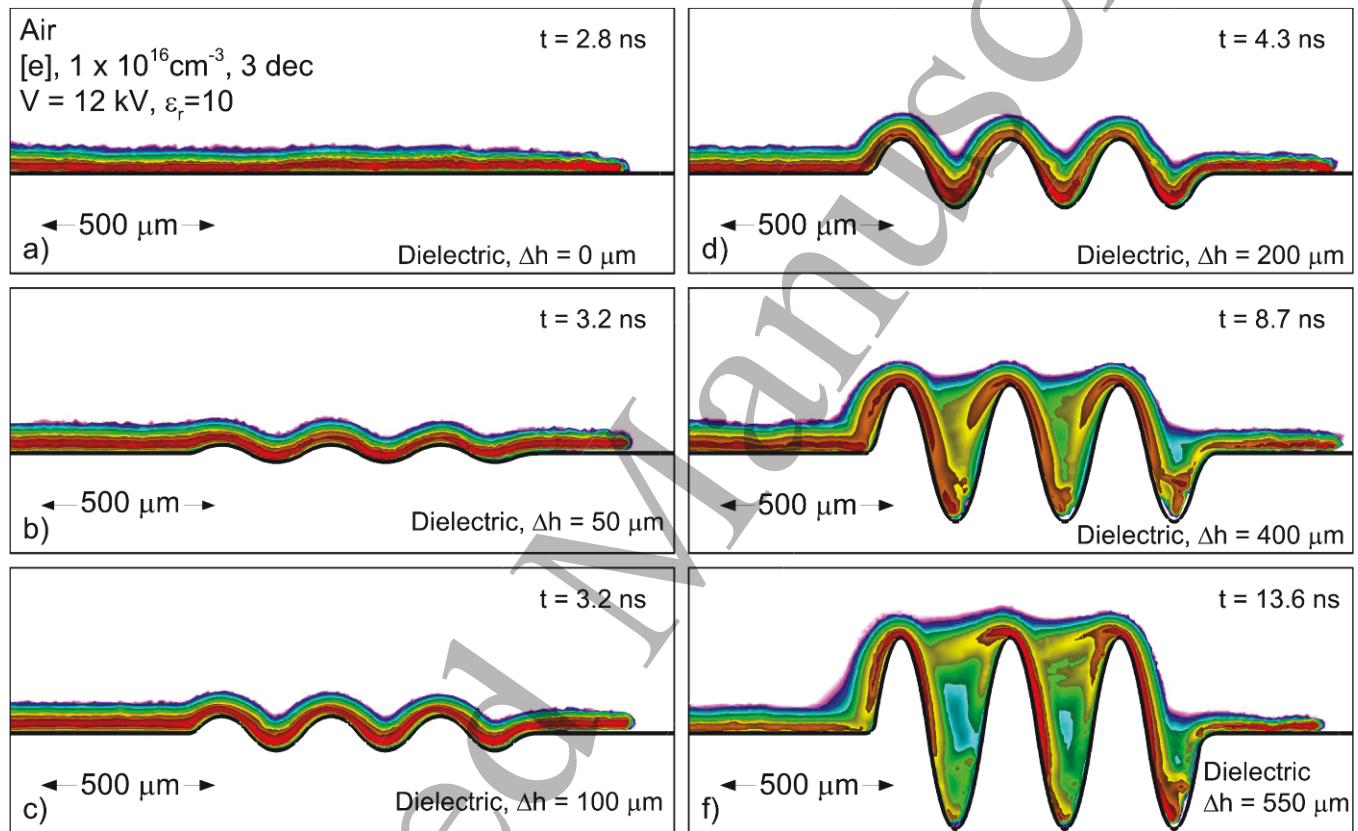
Konina, et al.
Fig 1 of 19

Air
[e], $1 \times 10^{13} - 3 \times 10^{15}$ cm^{-3}, log
$V = -12$ kV, $\varepsilon_r = 10$

t = 2.4 ns

500 μm

a)   Dielectric, Δh = 0 μm

t = 2.5 ns

500 μm

b)   Dielectric, Δh = 50 μm

t = 2.6 ns

500 μm

c)   Dielectric, Δh = 100 μm

t = 2.7 ns

500 μm

d)   Dielectric, Δh = 200 μm

t = 3.7 ns

500 μm

e)   Dielectric, Δh = 400 μm

t = 5.0 ns

500 μm

f)   Dielectric
                     Δh = 550 μm

Min   Max

Konina, et al.
Fig 3 of 19

S_e (1×10^{24}cm^{-3}s^{-1}, 4 dec)

[e] (2×10^{15}cm^{-3}, 3 dec)

←—— 500 μm ——→

t=1.4 ns

t=1.7 ns

t=1.9 ns

t=2.2 ns

t=2.8 ns

t=4.0 ns

Min ▭ Max

Konina, et al.
Fig 5 of 19

Air
[e], $1 \times 10^{16} cm^{-3}$, 3 dec
V = 12 kV, ε_r=10

a) 500 μm t = 2.8 ns Dielectric, Δh = 0 μm
b) 500 μm t = 3.2 ns Dielectric, Δh = 50 μm
c) 500 μm t = 3.2 ns Dielectric, Δh = 100 μm
d) 500 μm t = 4.3 ns Dielectric, Δh = 200 μm
e) 500 μm t = 8.7 ns Dielectric, Δh = 400 μm
f) 500 μm t = 13.6 ns Dielectric Δh = 550 μm

Konina, et al.
Fig 8 of 19

[e] (5x10^{13} cm^{-3}, 2 dec)   -30 kV   S$_e$ (5x10^{22}cm^{-3}s^{-1}, 3 dec)

a)   Dielectric Δh = 0 μm   16.5 ns   11.5 ns

b)   Dielectric Δh = 50 μm

c)   Dielectric Δh = 150 μm

d)   Dielectric Δh = 250 μm

Min   Max

Konina, et al.
Fig 11 of 19

[e]
$(5\times10^{13}$ cm^{-3}, 4 dec)

S_e
$(5\times10^{23}$cm^{-3}s^{-1},4 dec)

E/N (500 Td, linear)

250 μm

a)   11.0 ns

b)   11.5 ns

c)   12.5 ns

d)   13.5 ns

Min   Max   Min   Max

10^0 10^1 10^2 10^3 10^4 0   250   500

a)

b)

t = 1.8 ns ←— 400 µm —→ [e], 2 x 10^{16}cm^{-3} 3 dec, V = +12kv

t = 1.8 ns ←— 400 µm —→ S_e, 2 x 10^{25}cm^{-3}s^{-1} 4 dec, V = +12kv

t = 2.2 ns

t = 2.7 ns

t = 2.9 ns

t = 3.1 ns

Min ▮▮▮▮▮▮▮▮ Max

Konina, et al.
Fig 18 of 19